

Electromagnetic modeling of near-field phase-shifting contact lithography with broadband ultraviolet illumination

Fei Wang^a, Katherine E. Weaver^a, Akhlesh Lakhtakia^{a,b1} and Mark W. Horn^a

^a*CATMAS — Computational & Theoretical Materials Sciences Group, Department of Engineering Science & Mechanics, Pennsylvania State University, University Park, PA 16802-6812, USA*

^b*Photonics Section, Department of Physics, Imperial College London, London SW7 2BZ, UK*

Abstract. Near-field phase-shifting contact lithography is modeled to characterize electromagnetic absorption in a photoresist layer with one face in contact with a quartz binary phase-shift mask. The broadband ultraviolet illumination is represented as a frequency-spectrum of normally incident plane waves. A rigorous coupled-wave analysis is carried out to determine the absorption spectrum of the photoresist layer. The specific absorption rate in the photoresist layer is calculated and examined in relation to the geometric parameters. Columnar features in the photoresist layer are of higher quality on broadband illumination in contrast to monochromatic illumination, in conformity with some recent experimental results. Feature resolution and profile are noticeably affected by the depth of the grooves in the phase-shift mask. Ideally, the feature linewidth can be less than about 100 nm for broadband illumination in the transverse-magnetic mode. These conclusions are subject to modification by the photochemistry-wavelength characteristics of the photoresist.

Keywords: Contact lithography; Floquet harmonics; Linear polarization; Near field; Phase shift; Rigorous coupled-wave analysis; Specific absorption rate

¹Corresponding Author. Tel: +1-814-863-4319, Fax: +1-814-865-9974, e-mail: akhlesh@psu.edu

1 Introduction

Several near-field imaging techniques yielding sub-wavelength resolution have been recently reported [1]–[7]. In particular, *near-field phase-shifting contact lithography* has been demonstrated to extend the resolution of contact aligners to less than 200 nm by using single-layer photoresists with high aspect ratios [7, 8]. The aerial image generated by NFPSCL was suggested to be due to a combination of near-field and phase-shifting effects [4]. But features are resolved uniformly throughout photoresist layers of thicknesses far in excess of the exposure wavelength, which means that the dominance of near-field effects is doubtful and may even be absent [9]–[11]. In contrast, a recent experimental investigation on broadband ultraviolet (UV) lithography disclosed the high sensitivity of the feature resolution to the phase shifts built into the phase mask [8]. That phase-shifting effects are crucial to the success of NFPSCL while near-field effects are not always significant, was also confirmed by numerical simulation [13]. But one question still remains: why are the smallest linewidths achieved through NFPSCL with the use of broadband UV illumination, rather than with monochromatic illumination, particularly because of degradation of phase-shifting effects due to the presence of a wide spectrum in broadband illumination?

Electromagnetic modeling of NFPSCL has been carried out with different numerical methods by several researchers with different objectives. Aizenberg *et al.* [5] presented a simple model for the near-field effect but did not account for the phase-shifting effect. Kunz *et al.* [12] presented the finite-difference-time-domain (FDTD) modeling of NFPSCL on flexible substrates, focusing on top-surface imaging photoresists. More recently, we used the rigorous coupled-wave analysis (RCWA) to model electromagnetic absorption in the photoresist layer for monochromatic UV illumination [13]. We found that columnar features are transversely localized in the photoresist layer close to the edges of the periodically corrugated mask, as a result of the superposition of propagating Floquet harmonics. The evanescent Floquet harmonics play no role in this spatial localization.

The localization of absorption can be enhanced further by means of the superposition of many sets of propagating Floquet harmonics vibrating at different frequencies. In fact, preliminary modeling indicated noticeable improvement in feature resolution and profile on replacing monochromatic illumination by incoherent trichromatic illumination [13].

Motivated by those theoretical findings as well as by experimental data [8], we undertook the broadband-illumination modeling of NFPSCL, even though the commonplace industrial practice is to use quasimonochromatic (i.e., narrowband) illumination. Our results are reported here. As part of our technique, the electromagnetic field of the broadband source of illumination is represented by a superposition of plane waves of different frequencies and different wavevectors. The RCWA is performed to the variation of absorption with frequency at any location in the photoresist layer. The overall specific absorption rate (SAR) is then calculated to characterize the columnar features in the photoresist layer, which are certainly the precursors of aerial images obtained after development.

A significant conclusion is that broadband UV illumination can produce acceptable results, in contrast to the undesirable standing-wave patterns in the photoresist layer produced by monochromatic UV illumination. Even though the use of antireflection coatings (ARCs) can drastically reduce the standing-wave patterns, broadband illumination does not require the additional step of putting on an ARC; furthermore, filtering optics is also not needed with broadband illumination. We caution, however, that our electromagnetic modeling requires coupling with the spectral characteristics of the photochemistry of the photoresist, which coupling lies outside the scope of this paper; nevertheless, experimental results [8] are consistent with our conclusion.

2 Theoretical Analysis

The electromagnetic boundary value problem is schematically shown in Fig. 1. The three regions $0 < z < h_1$, $h_2 < z < h_3$, and $h_3 < z < h_4$ are occupied, respectively, by homogeneous materials labeled a , c , and d ; and the corresponding relative permittivity scalars are denoted by ϵ_a , ϵ_c , and ϵ_d . The region $h_1 < z < h_2$ acts as a binary phase-shift mask with alternate strips of widths qL and $(1-q)L$, $0 \leq q \leq 1$, made of materials labeled a and b . The half-spaces $z \leq 0$ and $z \geq h_4$ are vacuous. Material a is quartz, material b is air (equivalently, vacuum), material c is the chosen photoresist, while material d is silicon. For convenience, we define the thicknesses $\Delta h_j = h_j - h_{j-1}$, $j \in [1, 4]$, where $h_0 = 0$.

Broadband light is incident from the half-space $z \leq 0$ on to the plane $z = 0$. As a result, reflection and transmission into the two half-spaces, $z \leq 0$ and $z \geq h_4$, respectively, occur. The incident electromagnetic field is represented in the time-domain through the temporal Fourier transform as

$$\mathbf{E}_i(\mathbf{r}, t) = \int_{-\infty}^{\infty} \tilde{\mathbf{E}}_i(\mathbf{r}, \omega) e^{-i\omega t} d\omega, \quad \mathbf{H}_i(\mathbf{r}, t) = \int_{-\infty}^{\infty} \tilde{\mathbf{H}}_i(\mathbf{r}, \omega) e^{-i\omega t} d\omega, \quad (1)$$

where $\mathbf{r} = x\mathbf{u}_x + y\mathbf{u}_y + z\mathbf{u}_z$ and t represent the position vector and time, respectively, ω is the angular frequency, and $i = \sqrt{-1}$.

For compatibility with commonplace industrial usage, the field phasors $\tilde{\mathbf{E}}_i(\mathbf{r}, \omega)$ and $\tilde{\mathbf{H}}_i(\mathbf{r}, \omega)$ at any ω are taken to be associated with a plane wave propagating in the $+z$ direction; therefore,

$$\tilde{\mathbf{E}}_i(\mathbf{r}, \omega) = A(\omega) (a_s \mathbf{u}_y - a_p \mathbf{u}_x) \exp(ik_0 z), \quad (2)$$

$$\tilde{\mathbf{H}}_i(\mathbf{r}, \omega) = -\frac{1}{\eta_0} A(\omega) (a_s \mathbf{u}_x + a_p \mathbf{u}_y) \exp(ik_0 z), \quad (3)$$

where $I(\omega) = A^2(\omega)$ is the incident light's spectral intensity function, $\eta_0 = \sqrt{\mu_0/\epsilon_0}$ is the intrinsic impedance of vacuum, $k_0 = \omega\sqrt{\mu_0\epsilon_0} = 2\pi/\lambda_0$ is the vacuum wavenumber, and λ_0 is the wavelength in vacuum, μ_0 is the permeability of vacuum, and ϵ_0 is the permittivity of

vacuum. The amplitudes a_s and a_p determine the linear polarization state of the incident electromagnetic field, and are subject to the condition

$$a_s^2 + a_p^2 = 1. \quad (4)$$

As the total electromagnetic field everywhere is represented as

$$\mathbf{E}(\mathbf{r}, t) = \int_{-\infty}^{\infty} \tilde{\mathbf{E}}(\mathbf{r}, \omega) e^{-i\omega t} d\omega, \quad \mathbf{H}(\mathbf{r}, t) = \int_{-\infty}^{\infty} \tilde{\mathbf{H}}(\mathbf{r}, \omega) e^{-i\omega t} d\omega, \quad (5)$$

our next task is to calculate the field phasors $\tilde{\mathbf{E}}(\mathbf{r}, \omega)$ and $\tilde{\mathbf{H}}(\mathbf{r}, \omega)$ in terms of $\tilde{\mathbf{E}}_i(\mathbf{r}, \omega)$ and $\tilde{\mathbf{H}}_i(\mathbf{r}, \omega)$ for arbitrary ω and \mathbf{r} . Because of the planewave format of $\tilde{\mathbf{E}}_i(\mathbf{r}, \omega)$ and $\tilde{\mathbf{H}}_i(\mathbf{r}, \omega)$, the method of choice is RCWA.

Detailed accounts of RCWA are commonplace in the optics literature [14, 15]. As a complete account for the problem described via Figure 1 has been presented by us elsewhere [13], we just reproduce here the essence of the technique. Let the relative permittivity scalar be denoted by $\epsilon(\mathbf{r}, \omega)$. Because of

- (i) the x -periodicity of $\epsilon(\mathbf{r}, \omega)$ for $z \in (h_1, h_2)$, and
- (ii) the uniformity of $\epsilon(\mathbf{r}, \omega) \forall z \in (-\infty, \infty)$ along the y axis,

the total field phasors $\tilde{\mathbf{E}}(\mathbf{r}, \omega)$ and $\tilde{\mathbf{H}}(\mathbf{r}, \omega)$ can be decomposed everywhere in terms of Floquet harmonics as follows:

$$\tilde{\mathbf{E}}(\mathbf{r}, \omega) = \sum_{n \in \mathbb{Z}} \tilde{\mathbf{E}}^{(n)}(z, \omega) \exp\left(in \frac{2\pi x}{L}\right), \quad (6)$$

$$\tilde{\mathbf{H}}(\mathbf{r}, \omega) = \sum_{n \in \mathbb{Z}} \tilde{\mathbf{H}}^{(n)}(z, \omega) \exp\left(in \frac{2\pi x}{L}\right). \quad (7)$$

These field phasors must satisfy the frequency-domain Maxwell curl postulates everywhere.

Specifically, the equations

$$\left. \begin{aligned} \nabla \times \tilde{\mathbf{E}}(\mathbf{r}, \omega) &= i\omega\mu_0 \tilde{\mathbf{H}}(\mathbf{r}, \omega) \\ \nabla \times \tilde{\mathbf{H}}(\mathbf{r}, \omega) &= -i\omega\epsilon_0 \epsilon(\mathbf{r}, \omega) \tilde{\mathbf{E}}(\mathbf{r}, \omega) \end{aligned} \right\} \quad (8)$$

hold for $z \in (0, h_4)$. After expanding $\epsilon(\mathbf{r}, \omega)$ into a Fourier series with respect to x and substituting (6) and (7) into (8), the matrix ordinary differential equation

$$\frac{d}{dz} \left[\underline{\tilde{\mathbf{f}}}(z, \omega) \right] = i \left[\underline{\tilde{\mathbf{P}}}(z, \omega) \right] \left[\underline{\tilde{\mathbf{f}}}(z, \omega) \right] \quad (9)$$

is derived for $z \in (0, h_4)$, where the column vector $\left[\underline{\tilde{\mathbf{f}}}(z, \omega) \right]$ contains the x - and the y -directed components of both $\tilde{\mathbf{E}}^{(n)}(z, \omega)$ and $\tilde{\mathbf{H}}^{(n)}(z, \omega)$.

For digital computation, the restriction $|n| \leq N_t$ is necessary. Floquet expansions of the reflected field phasors in the half-space $z \leq 0$ and of the transmitted field phasors in the half-space $z \geq h_4$ are set up. Equation (9) is then solved, after enforcing the continuity of the x - and the y -directed components of the electromagnetic field phasors across the planes $z = 0$ and $z = h_4$. The parameter N_t has to be increased until a convergent solution of (9) is found [13].

Once the total field phasors $\tilde{\mathbf{E}}(\mathbf{r}, \omega)$ and $\tilde{\mathbf{H}}(\mathbf{r}, \omega)$ have been obtained everywhere by using RCWA, $\mathbf{E}(\mathbf{r}, t)$ and $\mathbf{H}(\mathbf{r}, t)$ can be determined from (5) for any \mathbf{r} and t by using the inverse Fourier transform. Our interest, however, lies only in the electromagnetic energy absorbed in the photoresist layer and converted into both thermal and chemical forms therein. Let the illumination be carried out only for $t \in [0, T]$. The (time-averaged) specific absorption rate SAR(\mathbf{r}) at a point \mathbf{r} is quantitated by

$$\text{SAR}(\mathbf{r}) = \omega \epsilon_0 \text{Im} [\epsilon(\mathbf{r}, \omega)] \frac{1}{T} \int_0^T \mathbf{E}(\mathbf{r}, t) \cdot \mathbf{E}(\mathbf{r}, t) dt, \quad (10)$$

for a quasimonochromatic field, with the assumption of no dispersion. In fact, when the field is monochromatic, i.e., $\mathbf{E}(\mathbf{r}, t) = \text{Re} \left[\tilde{\mathbf{E}}(\mathbf{r}) \exp(-i\omega t) \right]$, (10) yields the identity

$$\text{SAR}(\mathbf{r}) = \frac{1}{2} \omega \epsilon_0 \text{Im} [\epsilon(\mathbf{r}, \omega)] |\tilde{\mathbf{E}}(\mathbf{r})|^2, \quad (11)$$

which is well-known in the electromagnetics literature [16, Eq. 7-60]. If the temporal variation of $\mathbf{E}(\mathbf{r}, t)$ is known, for our purposes (10) may provide a proper, though not exact, estimation of $\text{SAR}(\mathbf{r})$. However, it is advantageous to represent $\text{SAR}(\mathbf{r})$ as a superposition of spectral dissipative contributions. In fact, according to Plancherel's theorem [17, p. 183]

$$\int_{-\infty}^{\infty} \mathbf{E}(\mathbf{r}, t) \cdot \mathbf{E}(\mathbf{r}, t) dt = \int_{-\infty}^{\infty} \tilde{\mathbf{E}}(\mathbf{r}, \omega) \cdot \tilde{\mathbf{E}}^*(\mathbf{r}, \omega) d\omega; \quad (12)$$

hence, we use the estimate

$$\text{SAR}(\mathbf{r}) \simeq \frac{1}{4\pi} (\omega_l + \omega_u) \epsilon_0 \int_{\omega_l}^{\omega_u} \omega \text{Im}[\epsilon(\mathbf{r}, \omega)] \tilde{\mathbf{E}}(\mathbf{r}, \omega) \cdot \tilde{\mathbf{E}}^*(\mathbf{r}, \omega) d\omega, \quad (13)$$

where ω_l and ω_u are two extremities of the frequency-band of $\tilde{\mathbf{E}}(\mathbf{r}, \omega)$. We implemented the right side of (13) in a representative element (RE) of material c , the RE being the $\Delta h_3 \times L$ rectangle in Fig. 1.

Absorption of photonic energy and subsequent curing together play a significant role in the formation of photoresist features after development. Therefore, the spatial characteristics of $\text{SAR}(\mathbf{r})$ provide direct information on the photoresist features developed — which, in other words, indicate pattern transfer from the mask (material a) to the photoresist layer (material c).

3 Results and Discussion

For illustrative results, we chose the following representative materials: material a is quartz with $\epsilon_a = 1.48^2$; material b is air so that $\epsilon_b = 1.0$; material c is the photoresist SPR 505 whose refractive index is plotted in Fig. 2(a) for $\lambda_0 \in [250, 610]$ nm [18]; material d is crystalline silicon whose refractive index is presented in Fig. 2(b) for $\lambda_0 \in [250, 610]$ nm [19]. In accordance with our earlier paper [13], the thicknesses $\Delta h_1 = 6$ mm, $\Delta h_3 = 1$ μm , and $\Delta h_4 = 1$ mm were chosen. While the thickness $\Delta h_2 = 460$ nm of the binary

phase-shift mask was fixed for most calculations, other values of Δh_2 were also adopted for comparative studies. Two values of L ($= 3$ and $4 \mu\text{m}$) and three values of the ratio q ($= 0.2, 0.5$ and 0.8) were chosen.

The broadband UV source was chosen to be of the UV400 type employed in commercial Süss Microtec mask aligners [20]. The spectral intensity function $I(\lambda_0)$ of this source is plotted in Fig. 3 for $\lambda_0 \in [250, 610]$ nm. This spectral regime was uniformly discretized into 136 subregimes, in each of which the electric field phasor $\tilde{\mathbf{E}}(\mathbf{r}, \omega)$ was represented with the value calculated at the central frequency of the subregime. Calculations of $\tilde{\mathbf{E}}(\mathbf{r}, \omega)$ were carried out after ascertaining that $N_t = 12$ sufficed to yield convergent results for all $\lambda_0 \in [250, 610]$ nm. As the incident light can be linearly linearly polarized, we set $a_s = 1$ for transverse electric (TE) fields and $a_p = 1$ for transverse magnetic (TM) fields, respectively.² We ensured that the principle of energy conservation was not violated by any of the results reported here [13].

Figs. 4–6 show gray-level (black implies low magnitudes, white implies high) plots of $\text{SAR}(\mathbf{r})$ throughout the representative element of the photoresist layer (see Fig. 1) for the three different values of q , when the illumination is broadband. Figs. 7–9 present the analogous $\text{SAR}(\mathbf{r})$ plots, but for monochromatic illumination of wavelength $\lambda_0 = 2(\sqrt{\epsilon_a} - 1)\Delta h_2 = 441$ nm. In all of these figures, the letter “Q” specifies an x -axis range of \mathbf{r} that is right underneath the strip of material a (quartz), while “A” specifies the range of \mathbf{r} underneath the strip of material of b (air). Results for both TE and TM illumination modes are presented in Figs. 4–9.

Clearly, the plots for the TE and TM illumination modes in Figs. 4–9 look quite different. The most prominent feature of Figs. 4–6, as compared with Figs. 7–9, is the enhanced localization of power dissipation, and the resulting improvement of black-colored columnar features. These columnar features denote those portions of the photoresist layer

²The electric (resp. magnetic) field of a TE (resp. TM) field does not have x - and z -directed components, and is thus directed parallel to the grooves of the phase-shift mask.

in which little electromagnetic energy is dissipated and therefore remain on the substrate after the development process. Our results indicate that, by using broadband UV light sources, the columnar features are dramatically localized underneath the vicinity of the phase edges (intersections) of the Q and A strips, while power dissipation occurs quite homogeneously outside the columnar features. In contrast, when the incident light is monochromatic, the columnar features are not resolved as nicely, which can be deduced from the presence of black-colored transverse strips in Figs. 7–9. The appearance of these strips is due to the standing-wave characteristic of the monochromatic field in the photoresist layer [13].

Undoubtedly, our theoretical results indicate that better feature resolution and profile would be achieved by using broadband illumination in place of monochromatic illumination. This conclusion coincides with the implications of recent experiments [8]. High-aspect-ratio columnar features are predicted by the model, especially for TM illumination, with linewidths less than 200 nm and profiles quite uniform on one side — as shown in Fig. 5(b).

Furthermore, the ratio q affects the position as well as the profile/resolution of the columnar features, which conclusion is arrived at on comparing Figs. 4 and 6 with Fig. 5. In particular, a large space between neighboring phase edges is helpful to isolate the photonic absorption features from each other, and thereby to localize the columnar features uniformly in the vertical direction. Therefore, a mid-value of q (i.e., $q \sim 0.5$) is suggested in order to obtain highly localized and uniform features.

The formation of columnar features is due to the spatial characteristics of propagating Floquet harmonics of the field phasors [13]. At a single frequency, these propagating Floquet harmonics discretely “beat” with each other to localize the electric field phasor transversely (i.e., along the x axis) in the photoresist layer. However, the electric field phasor has a longitudinal (i.e., along the z axis) standing-wave profile in the photoresist

layer, because of the spatial attributes of the propagating Floquet harmonics. On using broadband sources of illumination, the field phasors of many different frequencies enter the fray. In other words, Floquet harmonics of a range of frequencies are generated by the broadband source to collaboratively produce the total the electric field in the photoresist layer. Floquet harmonics of different frequencies correspond to different classes of both x - and z -variations; and the monochromatic standing-wave feature appears to be smoothed by the multifrequency Floquet harmonics. Therefore, the columnar features are highly localized, and photonic absorption in the remaining parts of the photoresist layer is highly uniformized, by broadband illumination. Of course, the standing-wave pattern would be even less pronounced, especially near the interface with silicon, by using an ARC that is index-matched to both the photoresist and silicon for broadband UV illumination — just as for monochromatic illumination [13].

In order to predict the features that might be developed in the photoresist layer, threshold modeling is often done. For instance, regions of the RE where the SAR is less than 10% of the maximum SAR are colored black to bring out the resolved features, while the remaining parts of the RE are colored white [13]. This has been done for the three SAR plots shown in Fig. 10. These were drawn for the same geometry as Figs. 5 and 8, for the TM illumination mode, and to show the differences between monochromatic and broadband illumination conditions. Furthermore, the normalization of SAR means that the plots are independent of the incident power density. The exposure wavelengths span the 250–610 nm range for Fig. 10(a), and the 300–440 nm range for Fig. 10(b), but $\lambda_0 = 441$ nm for Fig. 10(c). Clearly, high-aspect-ratio features of linewidth < 100 nm are uniformly well-resolved in the photoresist layer for the full broadband illumination, but not for the monochromatic illumination. Also, although we have not incorporated the photochemistry-wavelength response of the photoresist in our calculations, we can conclude that the standing-wave pattern of features is considerably diminished by the threshold (development) process for Fig. 10(a), but not for Fig 10(c) — which supports

the use of broadband illumination. Finally, the contrast between Figs. 10(a) and 10(b) implies the general effectiveness of the whole spectrum of UV400 illumination in resolving the patterned features.

Several geometrical factors influence the SAR distribution in the photoresist layer, and thereby the features developed. One factor is the period L of the phase-shift mask. Typically, large values of L are necessary for the formation of stable columnar features in the photoresist layer [13]. Figure 11 shows the same SAR distribution in the RE as Fig. 5, but for the shorter period $L = 3 \mu\text{m}$. Clearly, the columnar features present in Fig. 11 are not localized as uniformly as those in Fig. 5. In fact, our modeling suggests that $L \geq 4 \mu\text{m}$ is needed for the chosen broadband UV400 illumination.

Another influential factor is the thickness Δh_2 of the binary phase-shift mask. Experiments indicate that both the resolution and the profile of the photoresist features after development are very sensitive to the value of Δh_2 [8], so that smallest linewidths are only achieved at a critical value of $\Delta h_2 \pm 10 \text{ nm}$ on broadband UV illumination. Leaving aside the thermal and chemical aspects of NFPSCL, we think that electromagnetic modeling of SAR itself may provide a direct relationship between the groove depth and the columnar features localized in the photoresist layer. Figure 12 contains the SAR distributions in the RE calculated for different values of Δh_2 ranging from 350 nm to 550 nm, for TM-mode broadband UV400 illumination. Very clearly, the value of Δh_2 influences the SAR distribution so significantly that both highly and uniformly localized columnar features are present in the photoresist layer only for the restricted range $\Delta h_2 \in (400, 500) \text{ nm}$. Hence, the effect of Δh_2 on the NFPSCL performance should not be simply viewed as the phase-shift effect mentioned in Section 1. Instead, it would have to be understood in a framework that combines the phase-shifting behavior and the spatial field modulation due to the binary phase-shift mask [21].

4 Concluding remarks

In this paper, we theoretically analyzed photonic absorption in a photoresist layer employed in near-field phase-shifting contact lithography on broadband ultraviolet illumination. The electromagnetic field emitted by the broadband source was represented as a frequency-spectrum of normally incident plane waves, and a rigorous coupled-wave analysis was performed to obtain the absorption spectrum in the photoresist layer. The specific absorption rate was calculated to characterize the columnar features localized in the photoresist layer. The narrow columnar features realized suggest that high-aspect-ratio photoresist features can be printed on the silicon substrate after development — using broadband illumination — which is in accord with experimental observations as exemplified by Fig. 13 and Ref. 8.

Comparison with the results for monochromatic illumination reveals a dramatic improvement in the resolution and profile of columnar features by broadband illumination. Furthermore, TM illumination yields results of higher quality than TE illumination, with the smallest linewidth less than 100 nm after the threshold (development) process.

Our calculations indicate that the geometrical dimensions of the phase-shift mask influence the SAR distribution in the photoresist layer, and thereby the features developed. In particular, the shape ratio $q \sim 0.5$, and large values of period $L \geq 4 \mu\text{m}$, are needed for obtaining highly and uniformly localized columnar features in the photoresist layer. Furthermore, the groove depth Δh_2 affects the feature size and profile dramatically, so that restricted values of Δh_2 are necessary for the development of sub-wavelength high-aspect-ratio features by NFPSCL conducted with broadband UV illumination.

Suppose that Δh_2 is fixed for a phase shift of π at some favored wavelength in the central region of the illumination spectrum (see Fig. 3.) The use of an ARC would definitely assist in the production of desired features by monochromatic illumination, as is common

knowledge in the lithography community. Our electromagnetic modeling indicates that as good results could be obtained with broadband illumination — which would eliminate the need not only for ARCs but also filtering optics. Although we did not incorporate here the spectral characteristics of the photochemical response of the photoresist, our conclusion is buttressed by the numerous experimental examples presented in Ref. 8 which naturally contained the photochemical effects.

Acknowledgements. The authors acknowledge the computing assistance provided by Abdul H. Aziz (Institute for High Performance Computing Applications, Penn State), as well as fruitful discussions with Martin Peckerar (University of Maryland). FW thanks the Penn State Weiss Graduate Program for a Dissertation Fellowship. This work was also supported in part by the US National Science Foundation and the US Defense Advanced Research Projects Agency.

References

- [1] Betzig E, Trautman JK: Near-field optics: Microscopy, spectroscopy, and surface modification beyond the diffraction limit. *Science* **257** (1992) 189–195
- [2] Bauch L, Bauer J, Dreger H, Lauche B, MehlißG, Rothe S: A new chromeless phase mask for the photolithography. *Microelectron. Eng.* **17** (1992) 87–92
- [3] Rogers JA, Paul KE, Jackman RJ, Whitesides GM: Using an elastomeric phase mask for sub-100 nm photolithography in the optical near field. *Appl. Phys. Lett.* **70** (1997) 2658–2660
- [4] Rogers JA, Paul KE, Jackman RJ, Whitesides GM: Generating similar to 90 nanometer features using near-field contact-mode photolithography with an elastomeric phase mask. *J. Vac. Sci. Technol. B* **16** (1998) 59–68
- [5] Aizenberg J, Rogers JA, Paul KE, Whitesides GM: Imaging the irradiance distribution in the optical near field. *Appl. Phys. Lett.* **71** (1997) 3773–3775
- [6] Schmid H, Biebyck H, Michel B, Martin OJF, Piller NB: Light-coupling masks: An alternative, lensless approach to high-resolution optical contact lithography. *J. Vac. Sci. Technol. B* **16** (1998) 3422–3425
- [7] Paulus M, Schmid H, Michel B, Martin OJF: Contrast mechanisms in high-resolution contact lithography: A comparative study. *Microelectron. Eng.* **57–58** (2001) 109–116
- [8] Dang H, Tan JLP, Horn MW: Sub-150 nm, high-aspect-ratio features using near-field phase-shifting contact lithography. *J. Vac. Sci. Technol. B* **21** (2003) 1143–1148
- [9] Tanaka S, Nakao M, Hatamura Y, Komuro M, Hiroshima H, Hatakeyama M: Printing sub-100 nanometer features near-field photolithography. *Jpn. J. Appl. Phys. Part 1* **37** (1998) 6739–6744

- [10] Tanaka S, Nakao M, Umeda M, Ito K, Nakamura S, Hatamura U: Simulation of near-field photolithography using the finite-difference time-domain method. *J. Appl. Phys.* **89** (2001) 3547–3553
- [11] Miyazaki J, Nakae A, Kusunose H, Yoshioka N, Wakamiya W, Murayama K: Effect of phase error on lithographic characteristics using attenuated phase-shifting mask. *Jpn. J. Appl. Phys. Part 1* **33** (1994) 6785–6789
- [12] Kunz RR, Rothschild M, Yeung MS: Large-area patterning of similar to 50 nm structures on flexible substrates using near-field 193 nm radiation. *J. Vac. Sci. Technol. B* **21** (2003) 78–81
- [13] Wang F, Horn MW, Lakhtakia A: Rigorous electromagnetic modeling of near-field phase-shifting contact lithography. *Microelectron. Eng.* **71** (2004) 34–53
- [14] Moharam MG, Gaylord TK: Diffraction analysis of dielectric surface-relief gratings. *J. Opt. Soc. Am.* **72** (1982) 1385–1392
- [15] Jarem JM, Banerjee PP: *Computational Methods for Electromagnetic and Optical Systems*. Marcel Dekker, New York 2000
- [16] Johnk CTA: *Engineering Electromagnetic Fields and Waves* Wiley. New York 1975
- [17] Evans LC: *Partial Differential Equations*, p. 183. American Mathematical Society, Providence, Rhode Island 1998
- [18] We thank Ron Synowicki of J.A. Woollam Co., 645 M Street, Suite 102, Lincoln, Nebraska 68508; www.jawoollam.com. The photoresist SPR 505 is manufactured by Shipley Company, a subsidiary of Rohm and Haas; www.electronic-materials.rohmhaas.com
- [19] *Properties of Silicon*, EMIS Datareviews Series No. 4, pp. 72–79. INSPEC, London, UK 1988

[20] We thank Jason Adams of Süss MicroTec, 228 Suss Drive, Waterbury Center, Vermont 05677; www.suss.com

[21] Goodman JW: Introduction to Fourier Optics. McGraw–Hill, New York 1996

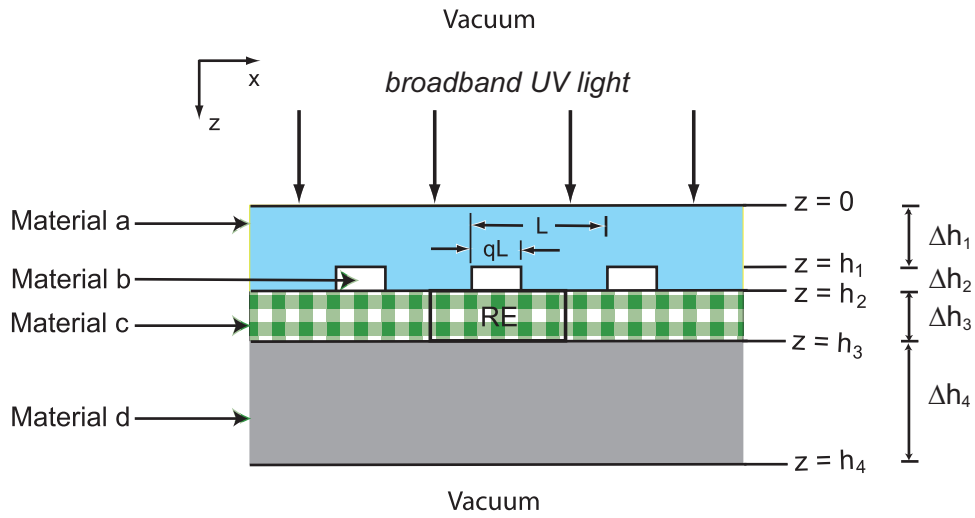


Figure 1: Schematic of the boundary value problem. SAR distributions in the region identified as the representative element (RE) are plotted in Figures 4–12. The length of the RE equals the period L , while its height is Δh_3 .

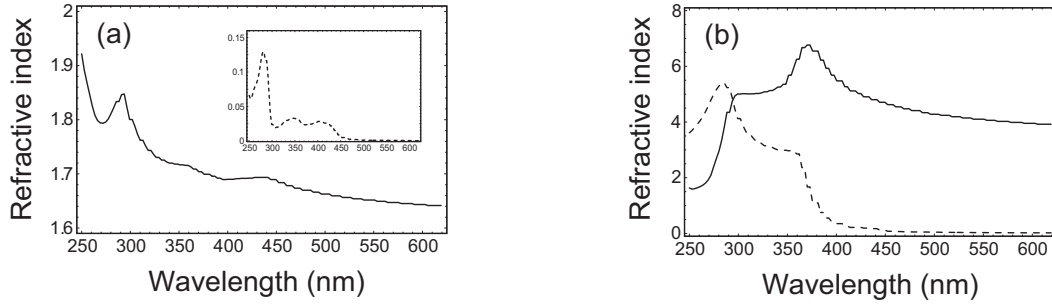


Figure 2: Real (solid lines) and imaginary (dashed lines) parts of the refractive index as functions of $\lambda_0 \in [250, 610]$ nm for (a) Photoresist SPR 505 and (b) crystalline silicon. The relative permittivity scalar is the square of the refractive index.

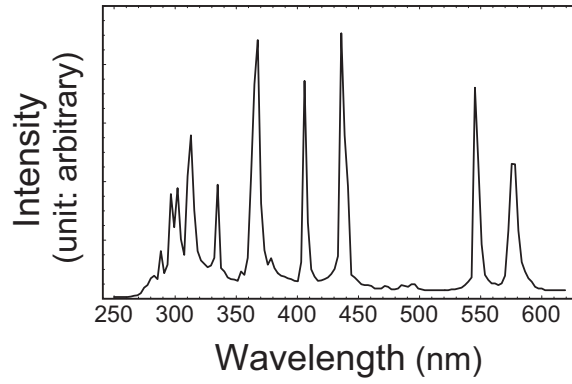


Figure 3: Spectral intensity $I(\lambda_0)$ of the UV400 source employed in commercial Süss MicroTec mask aligners [20]. Subsequent filtering for quasimonochromatic transmission at 313, 365 or 435 nm wavelength is often carried out, in standard lithography practice. The UV300 source made by the same company has an additional “dark lens”. For all broadband calculations presented here, the entire spectrum of the UV400 source, as shown in this figure, was used.

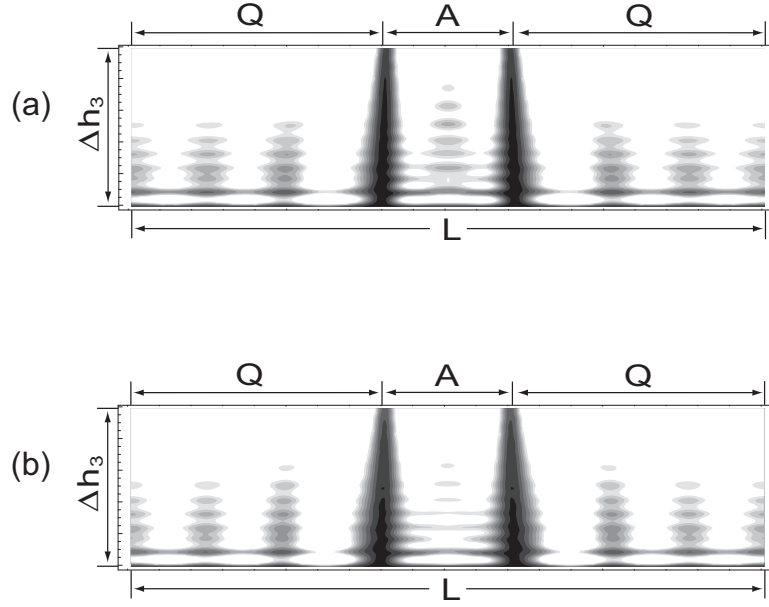


Figure 4: SAR distribution in the representative element (RE) of the photoresist layer for broadband illumination ($250 \leq \lambda_0 \leq 610$ nm) for (a) TE and (b) TM polarizations. The parameters $\Delta h_2 = 460$ nm, $\Delta h_3 = 1$ μm , $L = 4$ μm , and $q = 0.2$ were employed for calculation; and a gray-level contour plot of the SAR was presented by nine gray scales, where black denotes low levels and white denotes high levels.

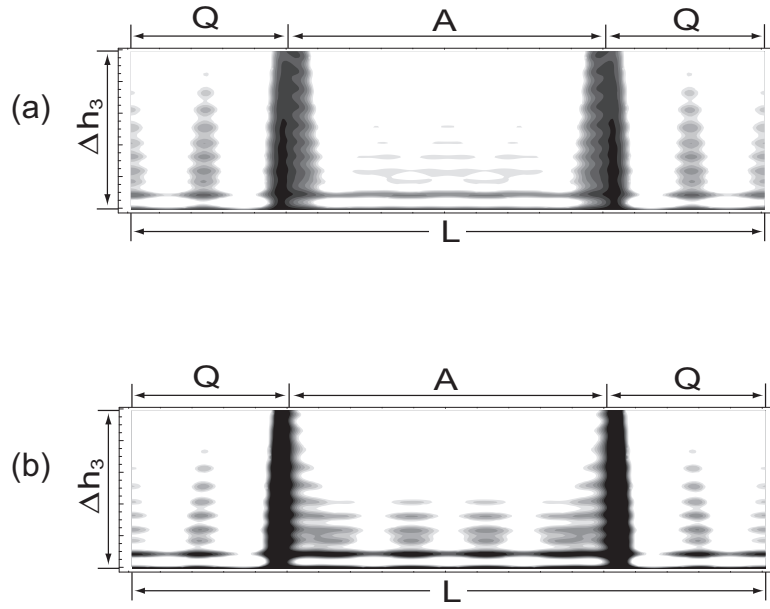


Figure 5: Same as Figure 4 but for $q = 0.5$.

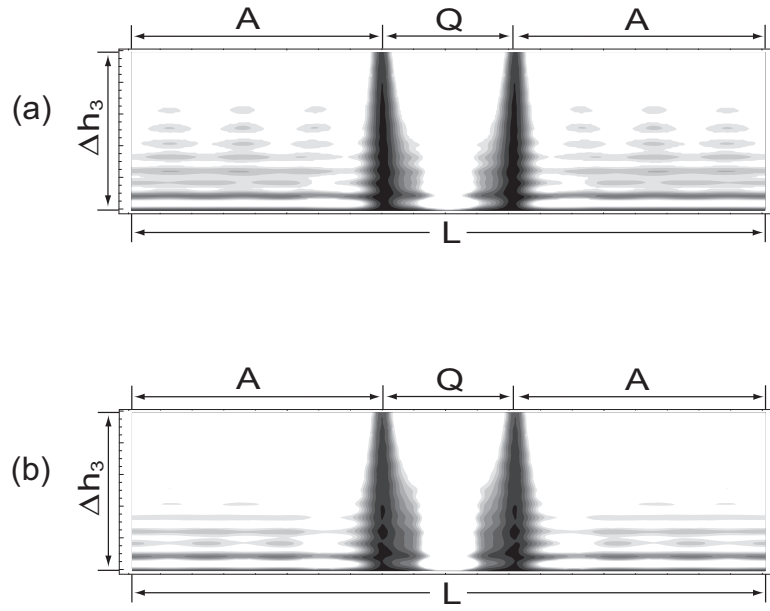


Figure 6: Same as Figure 4 but for $q = 0.8$.

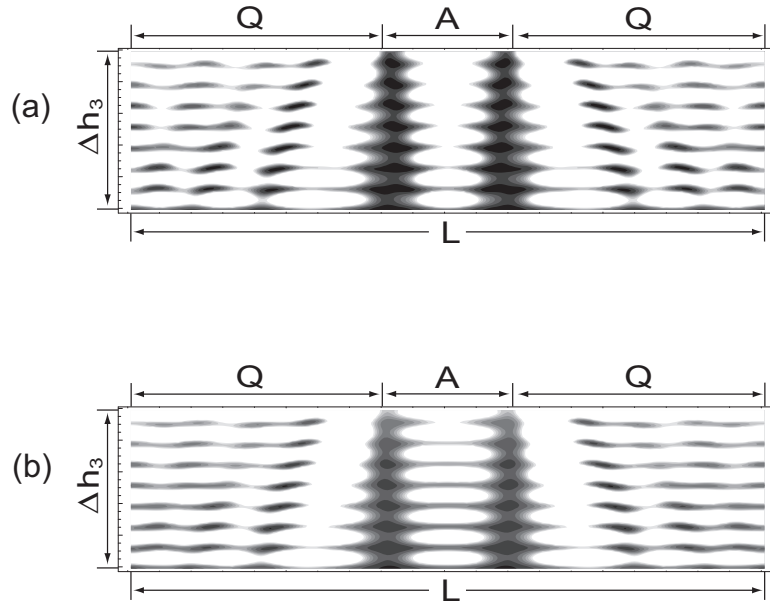


Figure 7: Same as Figure 4 but for monochromatic illumination at $\lambda_0 = 441$ nm.

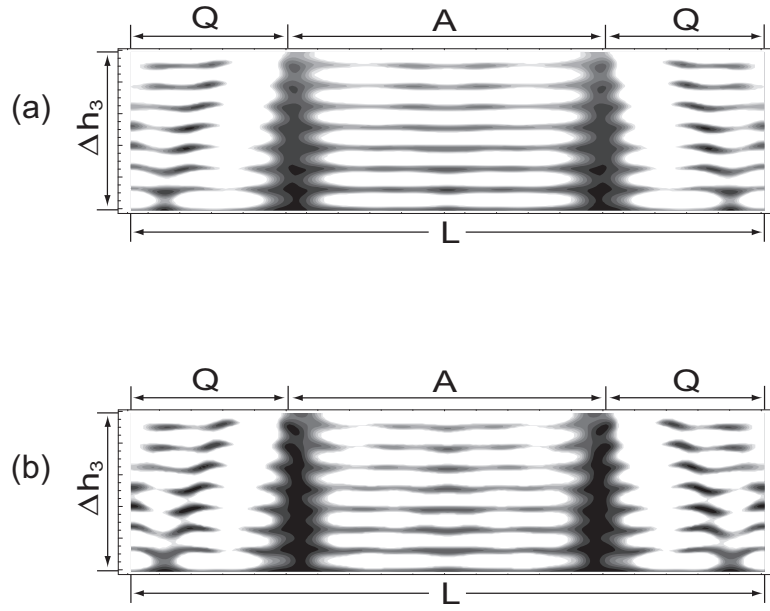


Figure 8: Same as Figure 7 but for $q = 0.5$.

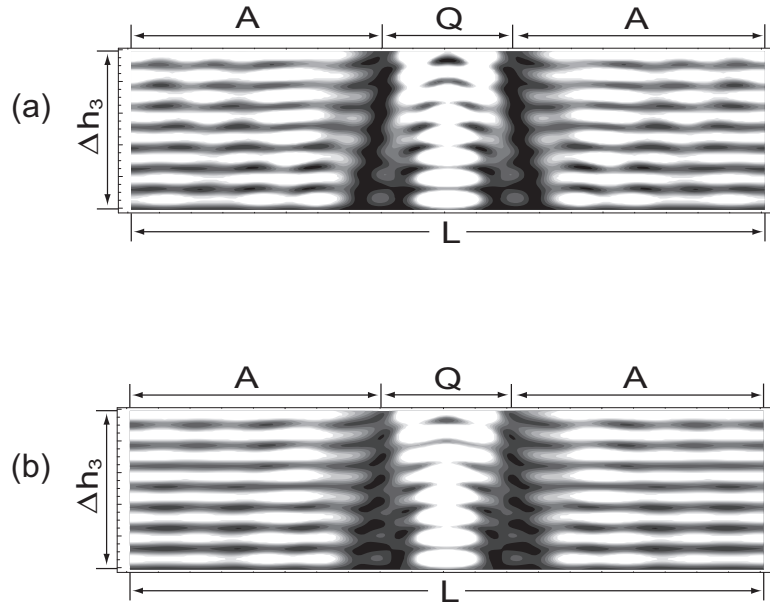


Figure 9: Same as Figure 7 but for $q = 0.8$.

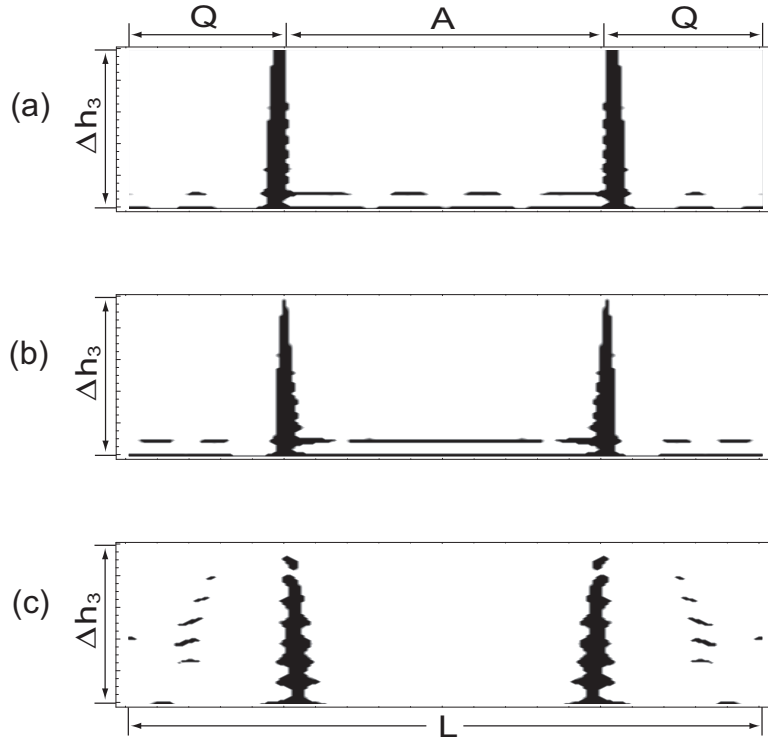


Figure 10: Post-thresholding SAR plots for TM illumination mode. (a) $250 \leq \lambda_0 \leq 610$ nm, (b) $300 \leq \lambda_0 \leq 440$ nm, and (c) $\lambda_0 = 441$ nm. The remaining parameters are the same as for Figures 5 and 8. Black-colored features correspond to SAR less than 10% of the maximum SAR, while the white-colored regions are for SAR exceeding 10% of the maximum SAR.

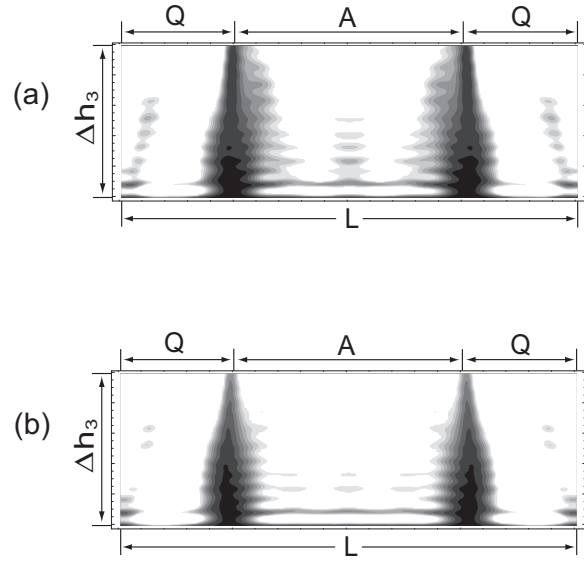


Figure 11: Same as Figure 5 but for $L = 3 \mu\text{m}$.

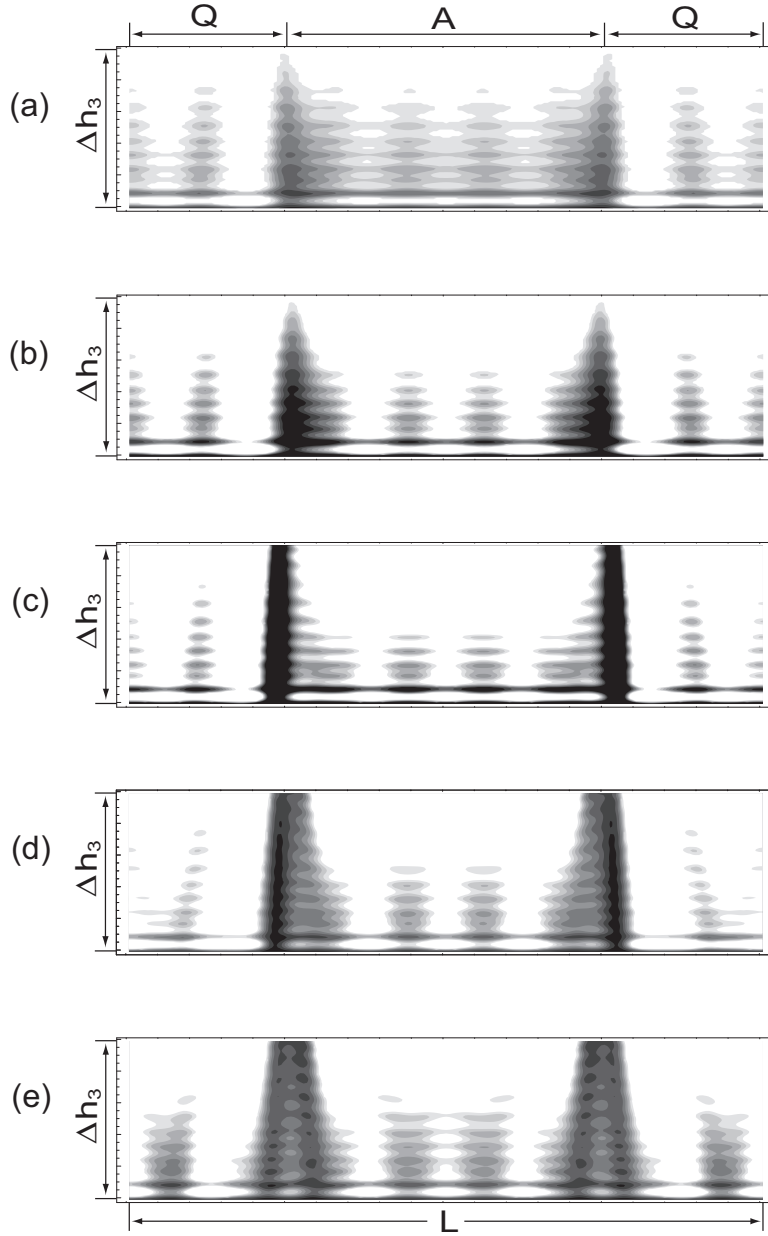


Figure 12: Same as Figure 5(b) but for different values of Δh_2 . (a) $\Delta h_2 = 350$ nm, (b) $\Delta h_2 = 400$ nm, (c) $\Delta h_2 = 460$ nm, (d) $\Delta h_2 = 500$ nm, and (e) $\Delta h_2 = 550$ nm.

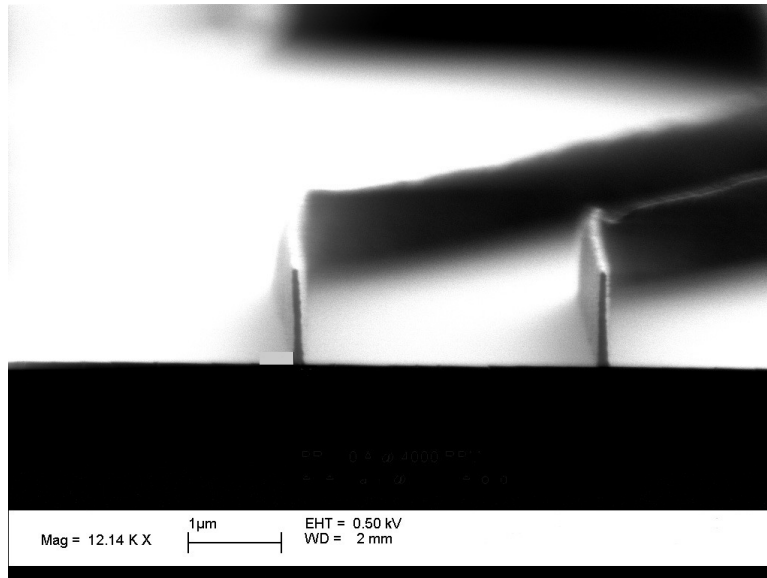


Figure 13: Two high-aspect-ratio features printed in SPR 510 using a chromeless phase-shifting mask, broadband illumination, and vacuum contact. Exposure time was 12.5 s, while the UV400 source was used without any filtering optics.